Title: Undrained cyclic loading behavior of stiff Eocene-to-Jurassic plastic, high OCR, clays

K. Pan, G. Y. Zhou, Z. X. Yang, and R. J. Jardine

Author 1: K. Pan, PhD
Associate Professor, College of Civil Engineering, Zhejiang University of Technology, Zhejiang, P. R. China

Author 2: G. Y. Zhou
Formerly, Graduate student, Polytechnic Institute, Zhejiang University, Zhejiang, P. R. China

Author 3: Z. X. Yang, PhD
Professor, Department of Civil Engineering, Zhejiang University, Zhejiang, P. R. China

Author 4: R. J. Jardine, PhD
Professor, Department of Civil and Environmental Engineering, Imperial College London, London, UK

Correspondence can be addressed to:

Z.X. Yang, PhD, Professor
Department of Civil Engineering,
Zhejiang University,
B712 Anzhong Building, Zijingang campus,
Hangzhou 310058, China
Email: zxyang@zju.edu.cn
Tel: +86 571 88208476

**Undrained cyclic loading behavior of stiff Eocene-to-Jurassic plastic, high OCR, clays**


**Abstract**

Assessing foundation response to cyclic loading is vital when designing transport infrastructure, such as road pavements and rail tracks, as well as offshore, port, and tall tower structures. While detailed guidance is available on characterizing many soil types' cyclic behavior, relatively few studies have been reported on stiff, geologically aged, plastic clays. This paper addresses this gap in knowledge by reporting cyclic loading experiments on three natural stiff UK clays that were deposited and buried between the Jurassic Age and Eocene Epoch before geological unloading to their currently heavily over-consolidated states. High-quality samples taken at relatively shallow depths were reconsolidated to nominally in-situ $K_0$ stresses in triaxial and hollow cylinder apparatus before imposing cyclic loading. The completely stable, metastable, or unstable outcomes invoked by different levels of undrained cyclic loading are interpreted within a kinematic yielding framework that is compatible with monotonic control experiments' outcomes. The cyclic limits marking the onset of significant changes in permanent strain accumulation, pore pressure development, and stress-strain hysteresis demonstrate that the weathered Gault clay offers the lowest cyclic resistance. The experiments show that energy considerations provide a promising way of evaluating undrained pore pressure generation and stiffness degradation. They also provide a basis for developing cyclic constitutive models and analysis procedures for cyclic foundation design in stiff, high OCR, plastic clay strata.



**Keywords:** Stiff clay; cyclic response; yielding; $K_0$ consolidation; stiffness degradation

## Introduction

Assessment of how subgrade soils respond to cyclic loading is vital to earthquake resistant design, see Idriss et al (1978) or Ishihara (1993). It is also often important to foundation analyses of transport infrastructure, such as railways, highways, and metro lines as well as offshore, port and other structures; Brown (1996), Gräbe and Clayton (2009), Andersen (2009), Jardine et al. (2012) or Wichtmann et al. (2013). Cyclic loading generally leads to the accumulation of permanent strains and, if undrained, excess pore-water pressure generation in soils which degrade shear strength and stiffness and may reduce foundation bearing capacity. The effects of undrained cyclic shearing on sands (e.g., Georgiannou and Konstadinou 2014; Pan et al. 2022) and low OCR clay sediments (e.g., Chu et al. 2002; Andersen 2015) have been investigated extensively through stress-path laboratory experiments. These studies, along with others, have identified how the cyclic responses of soils are governed by their composition (grading characteristics, plasticity), micro-structures, and state (void ratio, effective stress levels, over-consolidation ratio OCR) as well as the loading paths, including degrees of Principal Stress axis Rotation (PSR). Various permanent accumulation or degradation models have been developed considering the impacts of varying cyclic stress/strain levels and continuing to large numbers of load cycles (Vucetic and Dobry 1988; Matasovic and Vucetic 1995; Puppala et al. 2009; Tsai et al. 2014; Cai et al. 2018). For example, Cai et al. (2018) proposed a novel experimental approach to explore the cyclic responses of intact soft clay to traffic loading over many repeated cycles and reported high-quality data that could explain the observed settlement trends of ground.

The above listed experimental studies focused principally on soft postglacial, low to medium

OCR clays consolidated to $K_0$ (= $\sigma_h'/\sigma_z'$) ≤ 1, where $\sigma_h'$ and $\sigma_z'$ are the in-situ horizontal and vertical effective stresses, respectively. While studies have been reported recently on the cyclic behaviour of stiff low plasticity glacial tills (Ushev and Jardine 2022a, b), far less attention has been given to how regular undrained cycling influences high OCR, stiff plastic, geologically old clays, which are encountered worldwide. Examples include the Pleistocene clays found in the Merkel valley of Northern Alberta (Nasmith 1964), the Palaeogene Femern clays of Denmark and Germany (Heilmann-Clausen et al. 1984), the scaly clays of California, Italy, Malaysia, and elsewhere (Vannucchi et al. 2003), the Beaumont clays of Texas (Focht and Sullivan 1969), and the clay softrocks of Japan (Tatsuoka et al. 1997). Wilkinson (2011) and Brosse (2012) noted that stiff to hard clays deposited from the Triassic to the Eocene cover approximately 50% of the southern UK and outcrop under sections of the west-east and north-south high-speed railway lines and major highways that radiate out of London. These strata are also found at multiple UK and Belgian offshore windfarm sites and extend onshore over much of Northern France and Belgium. These stiff plastic clay strata experienced heavy prior loading due to their deposition and burial under potentially hundreds of meters of sediment, followed by marked erosion-induced over-consolidation, weathering in-situ and often more recent re-loading combined with vegetation. The layers encountered at shallow depths are usually considered to have in-situ $K_0$ values exceeding unity, i.e., $\sigma_h' > \sigma_z'$, rather than the $K_0 < 1$ conditions expected in low OCR strata.

It is well known that PSR can affect soil responses very significantly; see Hight et al. (1983); Li and Selig (1996); Chai and Miura (2002); Nishimura et al. (2007); Xiao et al. (2014); Cai et al. (2017) or Brosse et al (2017a, b). PSR is implicit in many types of infrastructure loading and is particularly important when exploring the $K_0$-consolidated stiff clays' responses to vehicle traffic loading. Experimental options when undertaking cyclic wheel loading studies include applying either (i) simplified triaxial normal stress waveforms or (ii) more complex cyclic paths that match the recent work by Pan et al. (2021a) on the stiff Cretaceous (Gault) clay. Considering both the $K_0$ (> 1) effect and wheel loading stress path provides better insight into the permanent cyclic strain development and resilient behavior expected with such soils. However, a consistent and comprehensive experimental study of such clays' cyclic behavior has yet to be presented.

This paper contributes investigations into the cyclic behaviors of the London and Kimmeridge stiff, plastic, high-OCR clays, deposited in the Eocene Epoch (49–56 million years ago) and the upper Jurassic Age (151–156 million years ago), respectively, and integrates these with a related study of the similarly classified lower Cretaceous Gault clay (Pan et al. 2021a). These strata's geological and geotechnical characteristics were established by Gasparre et al. (2007a), Wilkinson (2011), and Brosse (2012) through systematic laboratory and field experiments run at Imperial College London. Oedometer and triaxial shear tests by Hosseini Kamal (2012) showed these clays' broadly comparable compression and shear behaviors appeared relatively insensitive to their ages or burial depths. Instead, Hollow Cylinder Apparatus (HCA) and stress path triaxial tests showed how the natural clays' directionally oriented meso-structures and fissure discontinuities can affect their peak strength and post-peak brittleness profoundly (Nishimura et al. 2007; Gasparre et al. 2007b; Hosseini Kamal et al. 2014; Brosse et al. 2017b). Their nominally plane HCA tests identified how Lode's angle and anisotropy affect the clays' peak undrained shear strength $S_u$ and Mohr-Coulomb failure parameters, while large displacement experiments with ring-shear apparatus confirmed the marked brittleness of all three strata. Gasparre et al. (2007a) and

Brosse et al. (2017a) also showed that the clays' stiffnesses are markedly anisotropic, as illustrated by advanced small-strain triaxial monotonic and dynamic probing experiments and also HCA tests that cover the full non-linear range from very small strains to failure. Undrained horizontal loading leads to a far stiffer response than vertical loading, or horizontal shear loading.

The three stiff clays' monotonic shear response, especially their stiffness characteristics, have been interpreted within the kinematic yielding plasticity framework proposed by Jardine (1992), who identified two kinematic surfaces ($Y_1$ and $Y_2$) within the classical main yield surface ($Y_3$). The $Y_1$ surface marks the end of the linear-elastic region, within which the soil strains are perfectly linear without any movements at the particle contacts. High-resolution, locally instrumented, monotonic triaxial probing tests by Gasparre et al. (2007a) and Hosseini Kamal (2012) showed that the $Y_1$ region has approximately elliptical shape in $p'$-$q$ stress space and extends from about 0.001% to 0.002% axial strain. The $Y_2$ surface encompasses an area within which the stress-strain curve is non-linear but complete loading-unloading paths manifest both hysteresis and largely recoverable behavior. The energy dissipated with such hysteresis loops is attributed to small scale inter-particle yielding. Following research by Smith et al. (1992) on low OCR Bothkennar clay and Kuwano and Jardine (2007) on sands, Gasparre et al. (2007a) interpreted $Y_2$ yielding as occurring when strain increment directions changed during drained probing tests on London clay after achieving ≈0.04% axial strain when probing from $K_0$ conditions. The outer $Y_3$ surface corresponds to the conventional large-scale soil mechanics yield locus, which is associated with a significantly accelerated development of permanent strain, marked reduction in stiffness and often a marked tendency to dilate or contract (Jardine 1992).

Load cycling that engages the $Y_2$ kinematic yield surface leads to opened-up hysteretic loops and significant permanent straining. Pan et al. (2021a) correlated $Y_2$ yielding to the boundary between the stable and metastable cyclic responses shown by Gault clay. Ushev and Jardine (2022) reported similar outcomes from experiments on stiff low-plasticity glacial till and concluded that cycling within the $Y_2$ surface could lead to stable outcomes with negligible stiffness degradation and energy dissipation. This study considers the cyclic yielding characteristics of the stiff plastic London and Kimmeridge stiff clays through undrained cyclic triaxial (CT) and cyclic HCA (CHCA) tests reconsolidated to nominally in-situ stresses and synthesises the outcomes with Gault clay experiments by Pan et al. (2021a) and earlier studies of the clays' monotonic shearing behavior. The clays' cyclic permanent strain, pore pressure, and hysteretic stress-strain responses are classified as being either fully stable, metastable, or unstable, and cyclic $Y_2$ and $Y_3$ yielding are identified. The study provides a basis for constitutive modelling and analysis of cyclic design problems involving geologically aged, highly over-consolidated, stiff plastic clays.

## Sampling and soil properties

The Heathrow Airport Terminal 5 (London clay), Willow Brook Farm (Kimmeridge clay), and High Cross (Gault clay) sampling sites selected for this study cover strata deposited in broadly similar marine environments. Wilkinson (2011) summarized the detailed geological settings of the sampling locations. The samples were retrieved from blocks cut carefully in excavations or continuous wireline (triple barrel) Geobore-S rotary boreholes at different depths; Gasparre et al. (2007a) and Pan et al. (2021a) gave further details of the sampling procedures. Hosseini Kamal et al. (2014) showed that the two sampling methods lead to high-quality samples giving similar outcomes in parallel monotonic triaxial tests. The examined block London samples were taken 1.2 m below a clay surface from which 6 m of Quaternary gravel had been removed some decades earlier. The rotary core Kimmeridge samples ranged in depth from 8.56 to 13.08 m, respectively, while the Gault blocks were taken at 3.0 m, along with deeper rotary cores from 5.41 to 8.30 m depth. Table 1 summarizes the London and Kimmeridge clays' index properties and estimated $S_u$ from $K_0$-consolidated triaxial compression tests; the key aspects of the shallow and deep Gault samples' descriptions can be found in Pan et al. (2021a). While there are variations in index properties, the most significant differences relate to the soils' fabrics and meso-structures. The shallow Gault samples have the most intensive meso-fissures and discontinuities due to their additional desiccation by tree root action and chemical weathering, which is not evident in the more deeply buried Kimmeridge and London clay sampling locations. Wilkinson (2011) noted a major reduction in the degree of preferred particle orientation caused by weathering in the shallow Gault clay specimens.

Figure 1 presents, after Gasparre (2002) and Hosseini Kamal (2012), oedometer test results for natural samples derived from different depths that are compatible with the main study depth for each soil outlined above. The initial states of the compression curves reflect their in-situ void ratios. The oldest Kimmeridge clay (9.2 m depth) shows the lowest in-situ void ratio and compressibility, reflecting its plasticity and age (Table 1); while the weathered shallow (3.5 m) Gault clay has the highest compressibility and swelling coefficients. Hosseini Kamal (2012) identified the vertical yield stress $\sigma_{zy}'$ for the tested shallow/deep Gault and Kimmeridge samples as approximately 1.6, 2.0, and 2.2 MPa, respectively, while Gasparre (2005) estimated 1.0 MPa for the youngest (London clay) sample. Fig. 2 further compares the clays' monotonic undrained triaxial compression behaviors, reporting stress-strain curves and effective stress paths based on a London clay test conducted by the Authors and tests on the Kimmeridge and Gault clays by Hosseini Kamal (2012). The sampling depths and testing procedures were fully compatible for the four experiments considered. The shallow Gault sample was sheared after isotropic reconsolidation, while the others were reconsolidated to their in-situ $K_0$ states, as described subsequently, prior to undrained shearing. The test on London clay was reconsolidated to the effective stresses acting before the (fully drained) overlying gravel had been removed; it has both the highest effective stresses and $S_u$ of around 162 kPa. The Kimmeridge and Gault samples' $S_u$ correlate less directly with their effective stress levels or sampling depths, which were more affected by variations in the patterns of fissuring (Hosseini Kamal et al. 2014).

**Cyclic test procedures**

The cyclic experiments were performed with an advanced electromechanical triaxial testing system and a dynamic HCA manufactured by GDS Ltd; further apparatus details can be found in Wang et al. (2013) and Guo et al. (2018). The CT and CHCA tests employed 38 mm diameter, 76 mm high, specimens while those for HCA testing had 100 and 60 mm outer and inner diameters and were 200 mm high. The specimen preparation procedures followed Pan et al. (2021a). Gasparre et al. 2007(b) and Hosseini Kamal et al. (2014) addressed the specimen-size effects of natural stiff clays and concluded that triaxial and HCA tests on specimens with these diameters could offer acceptable consistency between their respective measurements. Fully saturated specimens were obtained by applying a back pressure of 600 kPa for 48 h while maintaining an effective confining pressure of 25 kPa.

The in-situ $K_0$ values assessed by Hosseini Kamal et al. (2014) and Brosse et al. (2017b) for the heavily over-consolidated Kimmeridge and Gault clays potentially varied from 3 to 1.5. However, the maximum $K_0$ that could be applied in laboratory experiments without generating excessive straining during triaxial reconsolidation was 1.8 and this value was adopted by Gasparre et al. (2007a) for London clay tests at comparable depths. Applying the same $K_0$ in conjunction with the measured water table depth and unit weight for each soil leads to the average in-situ effective stresses as depicted in Fig. 3 as points A', B', C', and D' in $p'$-$q$ coordinates. As noted by Gasparre et al. (2007a), the estimated in-situ stresses for the London sample take into account the 6 m of Quaternary Thames River Terrace gravels that had been removed prior to sampling. As shown in Fig. 3, specimens were first isotropically consolidated to their initial mean effective stress $p_0'$ levels and then extended to their estimated anisotropic stress points following constant $p'$ and drained paths. In both stages, sufficient pause periods were imposed until the axial creep strain rates stabilize to fall below the adopted 0.002%/h limit.

After anisotropic consolidation, cyclic loading waveforms outlined in Fig. 4 were applied at 1 Hz under undrained conditions. Following Li and Selig (1996) and Chai and Miura (2002), the CT experiments involved only the vertical stress waveform cycling sinusoidally from minima, representing in-situ $\sigma_z'$ stress, to maxima value of $\sigma_z'+\sigma_z^{cyc}$. In CHCA tests, the inner and outer cell pressures were kept constant, while the torsional shear stress $\tau_{z\theta}$ and vertical stress $\sigma_z$ were varied to follow the waveforms exemplified by Fig. 4 to match the cardioid ($\tau_{z\theta}$–$(\sigma_z$-$\sigma_\theta)/2$) incremental stress path shape considered by (1996) and Ishikawa et al. (2011) as matching wheel loading, where $\sigma_\theta$ is the circumferential stress. Tables 2 and 3 summarize the cyclic stress conditions applied in the CT and CHCA tests, respectively, as denoted by the normalized cyclic stress ratio CSR (= $\sigma_z^{cyc}/2p_0'$). All specimens were subjected to large numbers ($N$ = 10,000 to 50,000) of cycles, unless they failed with vertical strains exceeding 10% at earlier stages of cycling.

**Permanent vertical strain and pore pressure**

Figure 5 illustrates how vertical strains $\varepsilon_z$, which is the primary cause of highway surface settlement, developed in three of the seven CT tests and one CHCA experiment on London clay; also shown are the permanent strains $\varepsilon_z^p$ that developed over each cycle. The application of purely positive cycles of compressive stress in CT tests naturally leads to the specimens compressing axially. Figs. 6(a) and (b) bring together the London and Kimmeridge clays' $\varepsilon_z^p$–$N$ trends, respectively, considering all 14 CT-I and CT-II tests. The compressive strains developed in the three lowest CSR London clay and five lowest Kimmeridge cases tended to stabilize with $N$ over their later cyclic stages. The two highest CSR cycles applied to both clays led to marked strain accumulation and unstable responses after $2 < N < 300$ cycles in all four cases, with this being accompanied by shear band formation. The London clay CT tests conducted at CSR = 0.3 and 0.4 showed higher (although still comparatively modest) degrees of late-stage axial straining than the equivalent Kimmeridge cases.

It is notable that CHCA specimens subjected to the cardioid 'wheel loading' stress paths tended to extend axially rather than compress. Comparison of the equivalent CT and CHCA tests shown in Figs. 5(b) and (d) with identical CSRs indicate that cyclic PSR increases the absolute magnitudes of vertical straining as well as changing its sign. Gräbe and Clayton (2009) and Cai et al. (2017) reported similar trends from equivalent tests on low OCR sediments. This is because the initial decreasing $\sigma_z$ segment of each CHCA stress cycle (Fig. 4) brings the effective stress path first towards extension failure.

Figure 7(a) synthesizes the $\varepsilon_z^p$ strains developed at the $N$ = 100 and 50,000 stages in Fig. 6 and reveals three distinct deformation patterns, namely stable, metastable, and unstable. The $\varepsilon_z^p$ strains accumulated in CT-II tests on Kimmeridge samples appear negligibly small until CSR increases to 0.14, the upper cyclic threshold condition for the stable response, which is associated with $Y_2$ yielding (Jardine 1992). Cycles that engage the $Y_2$ surface lead to permanent straining and a metastable response that generates a linear growth of $\varepsilon_z^p$ with CSR up to CSR = 0.5, after which the $\varepsilon_z^p$ trend becomes sharply steeper, showing an unstable response. In the present study, the lower unstable threshold is interpreted as the $Y_3$ limit corresponding to the markedly accelerated accumulation rate of permanent (plastic) strain. Comparatively low threshold CSR values (0.1 and 0.45) are interpreted for the London clay, confirming lower cyclic resistance than that of the Kimmeridge clay. The CT-III and CT-IV tests' $\varepsilon_z^p$–CSR trends with respect to $N$ are further synthesized in Fig. 7(b), showing similar stable-to-metastable and metastable-to-unstable responses. As expected, the desiccation and weathering lead to the shallow weathered Gault clay exhibiting the lowest CSR limits (0.06 and 0.35), while marginally higher values (0.16 and 0.55) apply in the deep un-weathered Gault than to either the London or Kimmeridge specimens. The equivalent CHCA-III tests on deep Gault specimens (Fig. 7(c)) confirm that the deep Gault clay is more resistant to cyclic loading than the Kimmeridge, although the limited varying CSRs in CHCA-II tests preclude identifying clear region boundaries. However, the CHCA-III tests indicate distinctly lower CSR limits (0.1 and 0.25) than the corresponding triaxial tests because, as noted earlier, cyclic PSR leads to accelerated (and extensile) vertical straining. Cai et al. (2017) and Guo et al. (2018) conducted equivalent tests on low OCR, soft Wenzhou clay under identical cyclic loading conditions and reported distinctly lower threshold VCSRs (0.03 and 0.16) than the clays examined in this study. Their experiments confirmed that the Holocene Wenzhou clay has significantly lower cyclic resistance than the stiff, geologically aged, high OCR clays. Furthermore, the stiff clays were brittle and prone to develop shear bands at relatively low shear strength, a feature that was not observed in the Wenzhou clay, or the stiff glacial tills considered by Ushev and Jardine (2022a, b).

The excess pore-water pressure $u$ generated during undrained cycling is another important contributor to the (gradually draining) long-term service settlement of foundations, as background drainage of excess pore pressures lead to additional volumetric strains and settlements. The pore pressure development trends of three Kimmeridge specimens that exhibited typical stable, metastable, and unstable responses are presented in Fig. 8, in which the pore pressure ratio is normalized as $r_u = u/p_0'$ and the permanent $r_u^p$ is determined at the end of each cycle. Fig. 9 illustrates the corresponding changes in effective stress paths tracked at specified $N$ values, also showing the Kimmeridge clay's peak strength envelope identified by Hosseini Kamal (2012) from triaxial compression tests. Pore pressure measurement time lag effects make it unlikely that the effective stress path peaks and troughs were recorded accurately within any given cycle (see Ushev and Jardine 2022a), the paths plotted are considered indicative of the stress paths' directions of travel.

The stable strain response outlined previously manifests as a steady $r_u$–$N$ trend with only slight overall growth in $r_u^p$ (< 0.05, Fig. 8(a)) and relatively tight effective stress path loops with very limited reduction in $p'$ ($\Delta p'$ < 10 kPa, Fig. 9(a)). Undrained cycling that engages the $Y_2$ yield surface provokes a distinct increase in $r_u^p$ that appears to slow as $N$ grows (Figs. 8(b) and 9(b)) and lead to only slowly changing metastable effective stress paths. More significant pore pressure developments are found in tests involving higher CSRs that progress to unstable outcomes (Fig. 8(c)). The initial cyclic effective stress path moves leftward towards the compressive failure line, showing contractive behavior over the first 10,000 cycles (Fig. 9(c)). A rightward dilative shift follows after reaching $N$ = 10,000, leading to a slight decrease in the generated $r_u^p$. This behavior is consistent with the stiff high OCR clays' tendency to dilate when sheared monotonically to large strains under undrained conditions, with the effective stress path rotating markedly, as shown more clearly by Ushev and Jardine (2022a) for stiff glacial clay till through fully reliable local pore pressure measurements.

Figure 10 illustrates how the trends for $r_u^p$ with $N$ shown by each test series indicate three styles of pore pressure responses that match the CSR thresholds identified for the straining responses. Generally, pore pressure accumulation remains modest ($r_u^p$ < 0.05) within the stable regions and changes to increase approximately linearly with CSR after $Y_2$ yielding, indicating a metastable response. However, the $r_u^p$–CSR trends indicate less systematic trends over the unstable range of CSRs. The development rates of $r_u^p$ with respect to CSR can either accelerate or decelerate, or even change to negative, as is seen more clearly in the CHCA tests (Fig. 10(c)). As discussed previously, this is primarily due to the onset of dilatancy as cyclic failure approaches.

**Cyclic secant stiffness**

Gasparre et al. (2007a) reported how the natural London clay's non-linear monotonic stiffness degrades with strain after undergoing $Y_1$ yielding and shows more marked degradation with strain once the $Y_2$ surface is engaged. Rapid stiffness degradation after undergoing $Y_2$ yielding is also seen in the cyclic hysteretic stress-strain loops presented in Fig. 11. For the cyclic stress conditions considered herein, the stiffness represented by the undrained Young's ($E_{sec}^{u}$) and shear ($G_{sec}^{u}$) moduli are defined as the secant slope of the vertical and shear stress-strain backbone curves, respectively. The 'overall' strains presented in Figs. 11(a) and (c) represent the permanent strain trends, while the strain scales adopted in Figs. 11(b) and (d) have their strain origins re-zeroed at specified cycle numbers (i.e., $N$ = 1, 100, 1,000, 10,000, 50,000) to highlight changes in cyclic secant stiffness with increasing $N$. Stable tests that manifest nearly linear stress-strain curves display no significant hysteresis (Fig. 11(b)), while metastable tests provoke opened-up loops that rotate clockwise as $N$ increases, reflecting the marked stiffness degradation after $Y_2$ yielding (Fig. 11(d)).

Figure 12 illustrates directly how $E_{sec}^{u}$ (or $G_{sec}^{u}$) degrades with $N$ in different test series, showing both engineering unit and normalized degradation index $\delta$, which is defined as the ratio of Young's or shear moduli at cycle $N$ to their initial values at the first cycle (Idriss et al. 1978). The maximum $E_{sec}^{u}$ observed in the CT-I (= 125 MPa, Fig. 12(a)) and CT-II (= 137 MPa, Fig. 12(c)) tests, which did not involve high resolution local strain sensors, are marginally lower than the elastic $E_v^{u}$ obtained from static triaxial probing tests by Gasparre (2005) on the London clay (= 133 MPa) and by Brosse et al. (2017a) on the Kimmeridge (= 147 MPa) in tests employing high resolution local measurements. While applying higher CSRs in CT tests generates progressively lower $E_{sec}^{u}$ values and accelerates stiffness degradation, their tendency to fall with $N$ remains relatively modest. However, the CHCA-II tests shown in Fig. 12(e) reflect much steeper decays of $G_{sec}^{u}$ with increasing $N$, and the maximum value (= 56 MPa) found in the lowest CSR (= 0.074) test falls more significantly below the elastic $G_{hv}$ (=

70 MPa) reported by Brosse et al. (2017a). A generally linear relationship between $\delta$ and $N$ is found in Figs. 12(b), (d), and (f), which can be matched by the following semi-logarithmic expression:

$$\delta = 1 - a \ln N \tag{1}$$

where $a$ is a parameter dependent on the soil type and CSR. As depicted in Figs. 12(b) and (d), the parameter $a$ obtained from CT tests has an increasing trend under the stable and metastable ranges of CSR; similar increasing trends have been reported by Lee and Sheu (2007), Tsai et al. (2014), and Leng et al. (2017) on soft postglacial clays. However, it tends to significantly decrease as CSR further increases to induce cyclic failure under triaxial conditions. This behavior is not observed in the CHCA tests (see Fig. 12(f)), which indicate higher $a$ values. Another striking feature of the unstable CT tests' outcomes is that the dilatancy induced at the later cycling stages appears to significantly stiffen the clays' vertical cyclic response and consequently causes the $\delta$–ln$N$ trends to deviate from linearity.

The synthesized $\delta$ values applying over the last cycle plotted against CSR in Fig. 13 confirm the above noted distinctive styles of strain and pore pressure response. Stable tests show a slight degradation of nonlinear vertical or shear stiffness ($\delta$ > 0.93) under the applied cyclic loading within the $Y_2$ surface. While the trends developed in metastable or unstable CT tests show $\delta$ either decreasing gradually with CSR or falling modestly before stabilising, the CHCA experiments confirm more marked reductions of cyclic shear stiffness with $N$.

**Damping ratio and dissipated energy**

Figures 14(a) and (b) show the variations of damping ratio $\beta$, which is defined as the hysteretic area of the stress-strain loop (i.e., dissipated energy) to the equivalent elastic energy stored in each individual cycle, in CT-I and CT-II tests, respectively. Stable and metastable tests indicate a continuous falling trend of $\beta$ with respect to $N$ that can be expressed by the following power function:

$$\beta = b\left(N\right)^{-c} \tag{2}$$

The parameter $b$ depicted in Fig. 14 tends to increase with CSR, as symptomized by the upward-shifting of the best-fit (solid) lines in these logarithmic plots, while the exponent $c$ is decreasing with CSR and far below unity. Unstable tests exhibit relatively high $\beta$ values that have an overall decreasing trend with the applied $N$ but occasionally rise as the accelerated strain development with shear bands forming. The corresponding dissipated energy per unit volume $W$ in each cycle is plotted in Fig. 15 with respect to $N$ and CSR, showing comparable trends to those plotted for $\beta$ in Fig. 14. Cycling within the $Y_2$ limit leads to a modest and stable energy dissipation rate (< $10^{-3}$ kJ/m$^3$ per cycle), while unstable tests show very high dissipation rate (> 1 kJ/m$^3$). The metastable cases fall between these limits.

The increasing energy dissipation resulting from breakdown of fabric is a recognised feature of the cyclic degradation of soils (Kokusho 2013; Pan et al. 2021b). Figs. 16(a) and (b) present the variations of $E_{sec}^{u}$ and $r_u^{p}$, respectively, versus the corresponding cumulative energy $W$ from CT-I and CT-II tests at specified $N$ values (of 1, 100, and 10,000). The normalized $E_{sec}^{u}$–$W$ relationships plotted with semi-logarithmic axes (Fig. 16(a)) generally follow the linearly decreasing trend given by Eq. (3) for all three clays.

$$E_{\mathrm{sec}}^{\mathrm{u}} / p_0' = d - f\ln\left(W / p_0'\right) \tag{3}$$

The approximately parallel trends show parameter $f$ (≈ 69) over the whole cyclic loading process, while parameter $d$ increases with $N$. In Fig. 16(b), the cumulative energy associated with the generated pore pressure is expressed by the following power function:

$$r_u^p = m\left(W/p_0'\right)^n \tag{4}$$

Although there is experimental scatter, the parameters $m$ (= 0.15) and $n$ (= 0.32) appear to fit the tests irrespective of the clay stratum and $N$ value. Noting that a similar relationship between cyclic pore pressure and normalized energy has been reported for cohesionless soils by Konstadinou and Georgiannou (2013) and Pan and Yang (2020), the average $r_u^p$ curve from tests on isotropically and anisotropically consolidated Toyoura sand has been included for reference in Fig. 16(b). Considering energy dissipation appears to be an appropriate and fundamental step when characterising cyclic pore pressure generation in soils, adding to the conventional perspectives that employ stress and strain variables.

**Summary of cyclic yielding characteristics**

The cyclic test results outlined above can be classified as stable, metastable or unstable and be related to the clays' $Y_2$ and $Y_3$ yield surfaces. $Y_2$ yielding has been associated in this study with the onset of opening-up hysteretic loops that induce significant permanent straining. It is shown that tests involving cyclic stress that remain within the $Y_2$ surface tend to exhibit low and stable degrees of pore pressure generation ($r_u^p$ < 0.05), stiffness degradation ($\delta$ > 0.93), and energy dissipation ($W$ < $10^{-3}$ kJ/m$^3$ per cycle). The cyclic $Y_3$ limit is interpreted as the threshold CSR corresponding to rapid development of unstable irrecoverable straining and also rightward dilative shift of effective stress path during later cycling stages.

Figure 17 marks the loci followed (for each clay) by the peak points of the triaxial cyclic loading stress paths in batches of tests conducted with increasing CSR values as they rise from $K_0$ conditions to reach $Y_2$ and $Y_3$ yielding points. Also shown as solid lines are the characteristic points at which the undrained effective stress path changes from contractive to markedly dilative directions in monotonic tests. Cycling above the $Y_3$ yield points induces unstable outcomes and, given enough cycles, probably cyclic failure. When cycled from $K_0$ = 1.8 conditions, the deep Gault clay CT-III tests show the highest $q/p'$ ratios at cyclic $Y_3$ yielding, while the shallow Gault shows the lowest, presumably as a result of its desiccation and weathering.

The effective stress conditions at which undrained CHCA tests developed full cyclic failure are reported in Fig. 18 by plotting (as solid symbols) for each clay type the maximum ratios of $t$ (= $(\sigma_1'-\sigma_3')/2$) to $s'$ (= $(\sigma_1'+\sigma_3')/2$) and equivalent values of $\phi'$ (= $\sin^{-1}(t/s')$) against $\alpha$, defined as the $\sigma_1'$ orientation relative to the vertical axis. These failure points may be compared with the solid curves proposed from monotonic nominally plane strain HCA tests by Brosse et al. (2017b) on intact samples taken from ≈ 10 m depth. While the peak $t/s'$ conditions identified at cyclic failure for the Gault and Kimmeridge clays match the monotonic trends closely, the CHCA London clay test's failure point plots at a lower $t/s'$ than expected; this may be a consequence of its sampling depth or the presence of a sandy interlayer within this specimen.

## Conclusions

Several series of undrained cyclic tests have been conducted on high-quality $K_0$-consolidated samples of natural stiff Eocene-to-Jurassic clays to explore their deformation, pore pressure, and hysteretic responses to cyclic loading, including tests that apply 'wheel loading' stress paths involving PSR. These experiments provide comprehensive information on cyclic degradation behavior of stiff, high OCR clays. The main findings are summarized as follows.

1) The cyclic test outcomes can be interpreted within a kinematic yielding framework. While the stiff clays' responses are only truly elastic within a small $Y_1$ regions, their responses remain stable within far larger $Y_2$ surfaces, showing little discernible permanent straining and only minor pore pressure development. While stiffnesses degrade with number of cycles $N$, the damping ratios and dissipated energies remain low. Cycles that engage the $Y_2$ surface lead to metastable outcomes that generate progressively growing permanent strains and pore pressure, with more marked stiffness degradation and energy dissipation.

2) Once the cyclic paths engage their $Y_3$ yield surface, the stiff clays exhibit significantly accelerated permanent strain accumulation, rightward changes of effective stress path direction, or even cyclic failure. This style of response is deemed unstable. The cyclic $Y_2$ and $Y_3$ limits, which are interpreted as threshold cyclic stress ratios CSRs that divide the three main response patterns, fall within the yield surface identified from monotonic tests on the examined clays. The Kimmeridge clay shows greater resistance to cyclic loading than the London clay, while the shallow Gault appears to be the most prone to cyclic instability due to weathering effects.

3) Cyclic principal stress rotation significantly influences the stiff clays' metastable and unstable responses, leading to more rapid strain accumulation and stiffness decay in CHCA than in equivalent CT tests. In particular, the CHCA experiments conducted from $K_0$ = 1.8 conditions lead to axial extension rather than the compressive straining seen in CT tests.

4) The stiffness degradation and damping ratio trends of CT tests on the London and

Kimmeridge clays can be fitted over their stable and metastable ranges by empirical relationships that employ CSR-dependent parameters. The energy dissipated in specimens is also mathematically related to non-linear cyclic stiffness and pore pressure; the latter is uniquely correlated with cumulative energy during the whole loading process and is not affected by the applied CSR.

5) The cyclic tests also confirm the high OCR, stiff clays' tendency to undergo brittle failures involving shear band formation and a dilative tendency when sheared to large strains. The effective stress ratios $t/s'$ at which cyclic failure occurred in the CHCA tests were compatible with the outcomes of monotonic HCA experiments for two of the three tested clays. Once fully formed, the shear bands offer low shear resistances that must be recognized in practical engineering design.

Finally, the cyclic loading tests outlined above provide a basis for the analysis of cyclic problems involving geologically aged, high OCR, stiff plastic clays, which occur worldwide. They help guide the optimal design of foundations and drainage systems to reduce excessive ground movements during the service lives of highways, railtracks, and airport runways. Further studies are recommended to investigate how the dissipation of the cyclic pore pressures generated by wheel loading impacts the overall ground movements under long-term cyclic service loading. Additional laboratory testing on a wider range of geomaterials is also required to test the general applicability of the hypotheses proposed in this study regarding the application of kinematic-yielding and energy-based interpretive and modeling frameworks. However, the studies reported above provide general insights that can aid cyclic foundation design, as described for example by Andersen (2009), for other types of onshore and offshore structure built on comparable stiff, plastic clay strata.

## Declaration of competing interest

The authors declare that they have no known competing financial interests or personal relationships that could have appeared to influence the work reported in this paper.

## Data availability

Some or all data, models, and code that support the findings of this study are available from the corresponding author upon reasonable request.


## Acknowledgements

The research described was funded by the National Natural Science Foundation of China (Grant Nos. 52178362, 52020105003, and U2239251) and by the UK Royal Society Newton Advanced Fellowship NA160438 Award, which are acknowledged gratefully.


## Notations

| | |
|---|---|
| $a$, $b$, $c$, $d$, $f$, $m$, $n$ | empirical parameters |
| $E_{\mathrm{sec}}^{\mathrm{u}}$, $E_{\mathrm{v}}^{\mathrm{u}}$ | undrained cyclic secant and vertical Young's moduli, respectively |
| $e$ | void ratio |
| $G_{\mathrm{sec}}^{\mathrm{u}}$ | undrained shear secant modulus |
| $G_{\mathrm{hv}}$ | shear modulus in vertical plane |
| $K_0$ | coefficient of earth pressure |
| $N$ | number of loading cycles |

| | |
|---|---|
| $p'$, $p_0'$ | mean effective stress and initial mean effective stress, respectively |
| $q$, $q_0$ | deviatoric stress and initial deviatoric stress, respectively |
| $r_u$, $r_u^p$ | pore pressure ratio and permanent pore pressure ratio, respectively |
| $S_u$ | peak undrained shear strength |
| $u$ | excess pore-water pressure |
| $W$ | dissipated energy per unit volume |
| $w_n$ | natural water content |
| $\alpha$ | orientation of major principal stress relative to vertical axis |
| $\beta$ | damping ratio |
| $\delta$ | stiffness degradation index |
| $\varepsilon_z$, $\varepsilon_z^p$ | vertical strain and permanent vertical strain, respectively |
| $\sigma_1'$, $\sigma_3'$ | major and minor effective principal stresses, respectively |
| $\sigma_h'$, $\sigma_z'$ | horizontal and vertical effective stresses, respectively |
| $\sigma_z$, $\sigma_\theta$, $\tau_{z\theta}$ | vertical, circumferential, and shear stresses, respectively |
| $\sigma_z^{cyc}$, $\tau_{z\theta}^{cyc}$ | cyclic vertical and shear stress amplitudes, respectively |
| $\sigma_{zy}'$ | effective vertical yield stress |
| $\phi'$ | mobilized shear angle |

## References

Andersen, K. H. (2009). Bearing capacity under cyclic loading — offshore, along the coast, and on land. The 21st Bjerrum Lecture presented in Oslo, 23 November 2007. *Can. Geotech. J.*, 46 (5): 513–535.

Andersen, K. H. (2015). Cyclic soil parameters for offshore foundation design. *Frontiers in Offshore Geotechnics III*, London, Vol. 1, pp. 5–84.

Brosse, A. M. (2012). *Study of the anisotropy of three British mudrocks using a hollow cylinder apparatus*. London, UK: Imperial College.

Brosse, A. M., Hosseini Kamal, R., Jardine, R. J., and Coop, M. R. (2017a). The shear stiffness characteristics of four Eocene-to-Jurassic UK stiff clays. *Géotechnique*, 67 (3): 242–259.

Brosse, A. M., Jardine, R. J., and Nishimura, S. (2017b). The undrained shear strength anisotropy of four Jurassic to Eocene stiff clays. *Géotechnique*, 67 (8): 653–671.

Brown, S. F. (1996). Soil mechanics in pavement engineering. *Géotechnique*, 46 (3): 383–426.

Cai, Y. Q., Guo, L., Jardine, R. J., Yang, Z. X., and Wang, J. (2017). Stress-strain response of soft clay to traffic loading. *Géotechnique*, 67 (5): 446–451.

Cai, Y., Wu, T., Guo, L., and Wang, J. (2018). Stiffness degradation and plastic strain accumulation of clay under cyclic load with principal stress rotation and deviatoric stress variation. *J. Geotech. Geoenviron. Eng.*, 144 (5): 04018021.

Chai, J. C., and Miura, N. (2002). Traffic-load-induced permanent deformation of road on soft subsoil. *J. Geotech. Geoenviron. Eng.*, 128 (11): 907–916.

Chu, J., Bo, M. W., Chang, M. F., and Choa, V. (2002). Consolidation and permeability properties of Singapore marine clay. *J. Geotech. Geoenviron. Eng.*, 128 (9): 724–732.

Focht, J. A., and Sullivan, R. A. (1969). Two slides in overconsolidated Pleistocene clays. *Proc 7$^{th}$ Int. Conf. on Soil Mechanics and Foundation Engineering*, Mexico City, Vol 2, pp. 571–576.

Gasparre, A. (2005). *Advanced laboratory characterisation of London Clay*. London, UK: Imperial College.

Gasparre, A., Nishimura, S., Anh-Minh, N., Coop, M. R., and Jardine, R. J. (2007a). The stiffness of natural London Clay. *Géotechnique*, 57 (1): 33–47.

Gasparre, A., Nishimura, S., Coop, M. R., and Jardine, R. J. (2007b). The influence of structure on the behaviour of London Clay. *Géotechnique*, 57 (1): 19–31.

Georgiannou, V. N., and Konstadinou, M. (2014). Effects of density on cyclic behavior of anisotropically consolidated Ottawa sand under undrained torsional loading. *Géotechnique*, 64 (4): 287–302.

Gräbe, P. J., and Clayton, C. R. I. (2009). Effects of principal stress rotation on permanent deformation in rail track foundations. *J. Geotech. Geoenviron. Eng.*, 135 (4): 555–565.

Guo, L., Cai, Y. Q., Jardine, R. J., Yang, Z. X., and Wang, J. (2018). Undrained behaviour of intact soft clay under cyclic paths that match vehicle loading conditions. *Can. Geotech. J.*, 55 (1): 90–106.

Heilmann-Clausen, C., Nielsen, O. B., and Gersner, F. (1984). Lithostratigraphy and depositional environments in the Upper Paleocene and Eocene of Denmark. *B. Geol. Soc. Denmark*, 33: 287–323.

Hight, D. W., Gens, A., and Symes, M. J. (1983). The development of a new hollow cylinder apparatus for investigating the effects of principal stress rotation in soils. *Géotechnique*, 33 (4): 355–383.

Hosseini Kamal, R. (2012). *Experimental study of the geotechnical properties of UK mudrocks*. London, UK: Imperial College.

Hosseini Kamal, R., Coop, M. R., Jardine, R. J., and Brosse, A. (2014). The post-yield behaviour of four Eocene-to-Jurassic UK stiff clays. *Géotechnique*, 64 (8): 620–634.

Idriss, I. M., Dobry, R., and Singh, R. D. (1978). Nonlinear behavior of soft clays during cyclic loading. *J. Geotechn. Eng. Div.*, 104 (12): 1427–1447.

Ishihara, K. (1993). Liquefaction failure and flow during Earthquakes. 33rd Rankine Lecture. *Géotechnique*, 43 (3): 351–451.

Ishikawa, T., Sekine, E., and Miura, S. (2011). Cyclic deformation of granular material subjected to moving-wheel loads. *Can. Geotech. J.*, 48 (5): 691–703.

Jardine, R. J. (1992). Observations on the kinematic nature of soil stiffness at small strains. *Soils Found.*, 32 (2): 111–124.

Jardine, R.J., Andersen, K., and Puech, A. (2012). Cyclic loading of offshore piles: potential effects and practical design. Keynote Paper. *Proc 7th Int. Conf. on Offshore Site Investigations and Geotechnics*, SUT London, 59–100.

Kokusho, T. (2013). Liquefaction potential evaluations: Energy-based method versus stress-based method. *Can. Geotech. J.*, 50 (10): 1088–1099.

Konstadinou, M., and Georgiannou, V. N. (2013). Cyclic behaviour of loose anisotropically consolidated Ottawa sand under undrained torsional loading. *Géotechnique*, 63 (13): 1144–1158.

Kuwano, R., and Jardine, R. J. (2007). A triaxial investigation of kinematic yielding in sand. *Géotechnique*, 57 (7): 563–580.

Lee, C. J., and Sheu, S. F. (2007). The stiffness degradation and damping ratio evolution of Taipei silty clay under cyclic straining. *Soil Dyn. Earthq. Eng.*, 27 (8): 730–740.

Leng, J., Ye, G. L., Ye, B., and Jeng, D. S. (2017). Laboratory test and empirical model for shear modulus degradation of soft marine clays. *Ocean Eng.*, 146: 101–114.

Li, D. Q., and Selig, E. T. (1996). Cumulative plastic deformation for fine-grained subgrade soils. *J. Geotech. Eng.*, 122 (12): 1006–1013.

Matasovic, N., and Vucetic, M. (1995). Generalized cyclic-degradation-pore-pressure generation model for clays. *J. Geotech. Eng.*, 121 (1): 33–42.

Nasmith, H. (1964). Landlsides and Pleistocene deposits in the Meikle River valley in Northern Alberta. *Can. Geotech. J.*, 1 (3): 155–166.

Nishimura, S., Minh, N. A., and Jardine, R. J. (2007). Shear strength anisotropy of natural

London Clay. *Géotechnique*, 57 (1): 49–62.

Pan, K., Liu, X. M., Yang, Z. X., Jardine, R. J., and Cai, Y. Q. (2021a). Undrained cyclic response of K0–consolidated stiff cretaceous clay under wheel loading conditions. *J. Geotech. Geoenviron. Eng.*, 147 (8): 04021078.

Pan, K., Xu, T. T., Liao, D., and Yang, Z. X. (2022). Failure mechanisms of sand under asymmetrical cyclic loading conditions: experimental observation and constitutive modelling. *Géotechnique*, 72 (2): 162–175.

Pan, K., and Yang, Z.X. (2020). Evaluation of liquefaction potential of sand under random loading conditions: equivalent approach versus energy-based method. *J. Earthq. Eng.*, 24(1): 59–83.

Pan, K., Yang, Z. X., and Cai, Y. Q. (2021b). Flow liquefaction potential of loose sand: stress path envelope and energy–based evaluation. *Can. Geotech. J.*, 58 (11): 1783–1789.

Puppala, A. J., Saride, S., and Chomtid, S. (2009). Experimental and modeling studies of permanent strains of subgrade soils. *J. Geotech. Geoenviron. Eng.*, 135 (10): 1379–1389.

Smith, P. R., Jardine, R. J., and Hight, D. W. (1992). On the yielding of Bothkennar clay. *Géotechnique*, 42 (2): 257–274.

Tatsuoka, F., Ochi, K., Kohata, Y., and Wang, L. (1997). Experimental underground excavations in sedimentary softrock at Sagamihra. *Geotech. Eng.*, 125 (4): 206–223.

Tsai, C. C., Mejia, L.H., and Meymand, P. (2014). A strain-based procedure to estimate strength softening in saturated clays during earthquakes. *Soil Dyn. Earthq. Eng.*, 66: 191–198.

Ushev, E., and Jardine, R. J. (2022a). The behaviour of Bolders Bank glacial till under undrained cyclic loading. *Géotechnique*, 72 (1): 1–19.

Ushev, E., and Jardine, R. J. (2022b). The mechanical behaviour of Bolders Bank till. *Can.*

*Geotech. J.*, Published online, doi.org/10.1139/cgj-2021-0436.

Vannucchi, P., Maltman, A., Bettelli, G., and Clennel, B. (2003). On the nature of scaly fabric and scaly clay. *J. Struct. Geol.*, 25 (5): 673–688.

Vucetic, M., and Dobry, R. (1988). Degradation of marine clays under cyclic loading. *J. Geotech. Eng.*, 114 (2), 133–149.

Wang, J., Guo, L., Cai, Y. Q., Xu, C. J., and Gu, C. (2013). Strain and pore pressure development on soft marine clay in triaxial tests with a large number of cycles. *Ocean Eng.*, 74 (1): 125–132.

Wichtmann, T., Andersen, K. H., Sjursen, M. A., and Berre, T. (2013). Cyclic tests on high-quality undisturbed block samples of soft marine Norwegian clay. *Can. Geotech. J.*, 50 (4): 400–412.

Wilkinson, S. (2011). *The microstructure of UK mudrocks*. London, UK: Imperial College.

Xiao, J. H., Juang, C. H., Wei, K., and Xu, S. Q. (2014). Effects of principal stress rotation on the cumulative deformation of normally consolidated soft clay under subway traffic loading. *J. Geotech. Geoenviron. Eng.*, 140 (4): 04013046.

**Figure captions**

Fig. 1 Oedometer compression curves for natural samples from different depths

Fig. 2 (a) Stress-strain curves and (b) effective stress paths for natural clays in triaxial compression

Fig. 3 Reconsolidation stress path of specimens to their in-situ $K_0$ states

Fig. 4 Cyclic stress waveforms in CT and CHCA tests

Fig. 5 Vertical strain evolutions of London clay: (a) CT test with CSR = 0.115; (b) CT test with CSR = 0.250; (c) CT test with CSR = 0.558; (d) CHCA test with CSR = 0.250

Fig. 6 Permanent vertical strain of (a) London clay in CT-I tests and (b) Kimmeridge clay in CT-II tests

Fig. 7 Synthesis of $\varepsilon_z^p$ at specified *N* versus CSR: (a) CT-I and CT-II tests; (b) CT-III and CT-IV tests; (c) CHCA-II and CHCA-III tests

Fig. 8 Pore pressure development of Kimmeridge clay in CT-II tests: (a) CSR = 0.135; (b) CSR = 0.368; (c) CSR = 0.567

Fig. 9 Effective stress path of Kimmeridge clay in CT-II tests: (a) CSR = 0.135; (b) CSR = 0.368; (c) CSR = 0.567

Fig. 10 Synthesis of $r_u^p$ at specified *N* versus CSR: (a) CT-I and CT-II tests; (b) CT-III and CT-IV tests; (c) CHCA-II and CHCA-III tests

Fig. 11 Typical hysteretic response of Kimmeridge clay in CT-II tests: (a) and (c) complete vertical stress-strain loops; (b) and (d) re-zeroed vertical stress-strain loops at specified *N*

Fig. 12 Variation of cyclic secant modulus and stiffness degradation index with *N*: (a) and (b) London clay in CT-I tests; (c) and (d) Kimmeridge clay in CT-II tests; (e) and (f) Kimmeridge clay in CHCA-II tests

Fig.13 Variation of stiffness degradation index at the last cycle with CSR: (a) CT-I and CT-II tests; (b) CT-III and CT-IV tests; (c) CHCA-II and CHCA-III tests

Fig. 14 Variation of damping ratio with *N*: (a) London clay in CT-I tests; (b) Kimmeridge clay in CT-II tests

Fig. 15 Variation of dissipated energy per unit volume with *N*: (a) London clay in CT-I tests; (b) Kimmeridge clay in CT-II tests

Fig. 16 (a) Normalized relationship between cyclic secant stiffness and cumulative dissipated energy; (b) permanent pore pressure ratio against normalized cumulative energy

Fig. 17 Summary of cyclic yield limits interpreted from CT tests

Fig. 18 Variations of maximum stress ratio $t/s'$ with $\sigma_1'$ axis orientation $\alpha$ covering both monotonic and cyclic HCA tests

Table 1 Index properties of test materials

| Index property | London clay | Kimmeridge clay |
|---|---|---|
| Specific gravity, $G_s$ | 2.74 | 2.51 |
| Unit weight, $\gamma$ (kN/m$^3$) | 19.8-20.1 | 20.3-20.7 |
| Natural water content, $w_n$ (%) | 20.5-23.6 | 22.6-26.8 |
| Plastic limit, $w_p$ (%) | 25 | 23 |
| Liquid limit, $w_l$ (%) | 69 | 54 |
| Plasticity index, $I_P$ | 44 | 31 |
| Clay fraction (%) | 50-53 | 57-60 |
| Undrained shear strength, $S_u$ (kPa) | ≈162 | ≈82[a] |

[a] after Hosseini Kamal (2012)

Table 2 Summary of cyclic triaxial (CT) tests

| Series | Depth (m) | $w_n$ (%) | $\sigma_z^{cyc}$ (kPa) | CSR | $N$ | Response pattern |
|---|---|---|---|---|---|---|
| CT-I | 1.2 | 20.5 | 60 | 0.115 | 50000 | Metastable |
| (London clay) | 1.2 | 23.6 | 104 | 0.200 | 50000 | Metastable |
| | 1.2 | 21.6 | 130 | 0.250 | 50000 | Metastable |
| | 1.2 | 22.2 | 156 | 0.300 | 50000 | Metastable |
| | 1.2 | 23.1 | 208 | 0.400 | 50000 | Metastable |
| | 1.2 | 21.7 | 290 | 0.558 | 50000 | Unstable |
| | 1.2 | 22.4 | 380 | 0.730 | 47 | Unstable |
| CT-II | 13.08 | 26.8 | 30 | 0.074 | 50000 | Stable |
| (Kimmeridge | 12.77 | 25.8 | 55 | 0.135 | 50000 | Stable |
| clay) | 13.08 | 25.0 | 105 | 0.257 | 50000 | Metastable |
| | 12.77 | 24.9 | 150 | 0.368 | 50000 | Metastable |
| | 12.77 | 24.2 | 200 | 0.490 | 50000 | Metastable |
| | 13.08 | 26.3 | 230 | 0.567 | 50000 | Unstable |
| | 13.08 | 24.6 | 315 | 0.772 | 18 | Unstable |
| CT-III | 7.01 | 30.6 | 15.9 | 0.067 | 50000 | Stable |
| (deep Gault clay) | 7.01 | 30.5 | 21 | 0.088 | 50000 | Stable |
| | 7.01 | 30.5 | 30 | 0.127 | 50000 | Stable |
| | 7.38 | 27.1 | 60.5 | 0.256 | 50000 | Metastable |
| | 8.30 | 22.3 | 81 | 0.343 | 50000 | Metastable |
| | 7.38 | 27.3 | 88.5 | 0.375 | 50000 | Metastable |
| | 7.38 | 26.9 | 118.5 | 0.502 | 50000 | Metastable |
| | 8.30 | 22.8 | 141.6 | 0.600 | 50000 | Unstable |
| | 8.30 | 21.9 | 165 | 0.699 | 50000 | Unstable |
| CT-IV | 3.0 | 23.7 | 10.5 | 0.088 | 10000 | Metastable |
| (shallow Gault | 3.0 | 23.9 | 19.8 | 0.165 | 10000 | Metastable |
| clay) | 3.0 | 23.6 | 24.6 | 0.205 | 10000 | Metastable |
| | 3.0 | 23.2 | 29.4 | 0.245 | 10000 | Metastable |
| | 3.0 | 23.3 | 34.3 | 0.286 | 10000 | Metastable |
| | 3.0 | 22.8 | 36 | 0.300 | 10000 | Metastable |
| | 3.0 | 22.8 | 48 | 0.400 | 10000 | Unstable |
| | 3.0 | 23.6 | 54 | 0.450 | 10000 | Unstable |
| | 3.0 | 22.9 | 66 | 0.550 | 10000 | Unstable |
| | 3.0 | 23.3 | 78 | 0.650 | 10000 | Unstable |
| | 3.0 | 23.7 | 96 | 0.800 | 2280 | Unstable |

Table 3 Summary of cyclic hollow cylinder apparatus (CHCA) tests

| Series | Depth (m) | $w_n$ (%) | $\sigma_z^{cyc}$ (kPa) | $\tau_{z\theta}^{cyc}$ (kPa) | CSR | $N$ | Response pattern |
|---|---|---|---|---|---|---|---|
| CHCA-I (London clay) | 1.2 | 20.7 | 130 | 43.3 | 0.250 | 36 | Unstable |
| CHCA-II | 11.82 | 24.2 | 30 | 10 | 0.074 | 50000 | Metastable |
| (Kimmeridge clay) | 13.08 | 22.6 | 96 | 32 | 0.235 | 50000 | Unstable |
| | 8.56 | 24.6 | 183 | 61 | 0.449 | 308 | Unstable |
| CHCA-III | 7.38 | 22.4 | 15.9 | 5.3 | 0.067 | 50000 | Stable |
| (deep Gault clay) | 5.66 | 22.2 | 30 | 10 | 0.127 | 50000 | Metastable |
| | 5.41 | 22.1 | 53.1 | 17.7 | 0.225 | 50000 | Metastable |
| | 7.74 | 25.6 | 67.5 | 22.5 | 0.286 | 50000 | Unstable |
| | 7.99 | 30.2 | 81 | 27 | 0.343 | 50000 | Unstable |
| | 8.30 | 27.2 | 94.5 | 31.5 | 0.400 | 50000 | Unstable |
| | 7.01 | 29.8 | 106.2 | 35.4 | 0.450 | 5020 | Unstable |

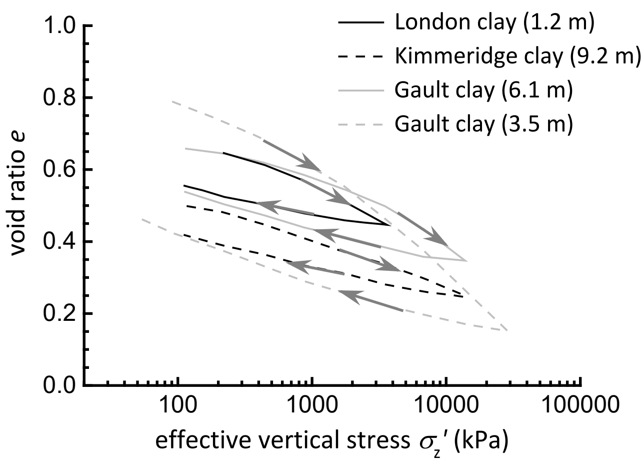


Fig. 1 Oedometer compression curves for natural samples from different depths (London clay data from Gasparre (2005); Kimmeridge and Gault clay data from Hosseini Kamal (2012))

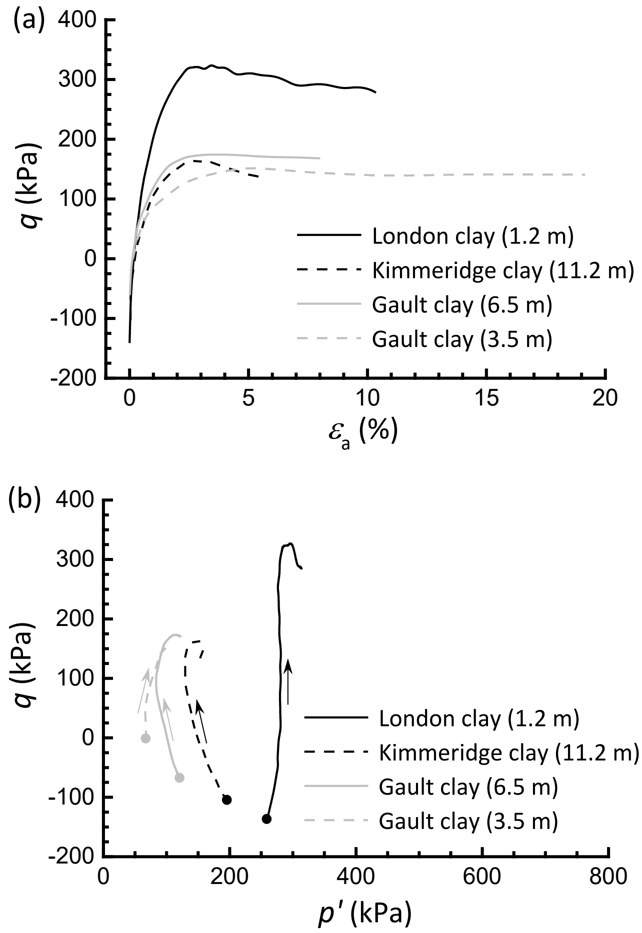


Fig. 2 (a) Stress-strain curves and (b) effective stress paths for natural clays in triaxial compression (Kimmeridge and Gault clay data from Hosseini Kamal (2012))

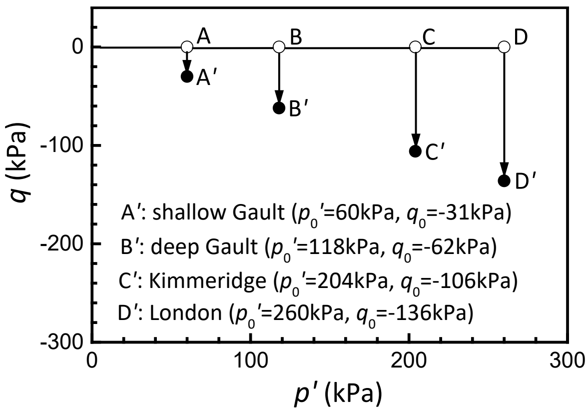


Fig. 3 Reconsolidation stress path of specimens to their in-situ $K_0$ states

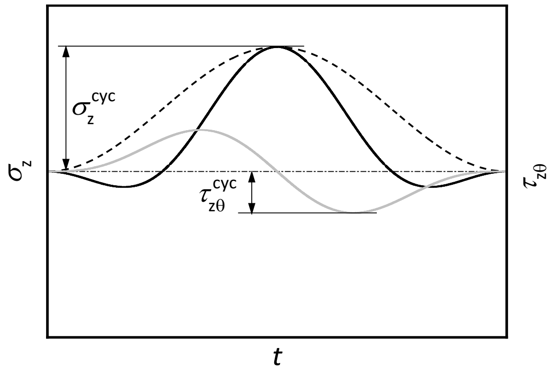


Fig. 4 Cyclic stress waveforms in CT and CHCA tests (Note: dash line represents $\sigma_z$ in CT test and solid lines represent $\sigma_z$ and $\tau_{z\theta}$ in CHCA test; the cyclic stress amplitude $\sigma_z^{cyc}/\tau_{z\theta}^{cyc}$ = 3 in CHCA test)

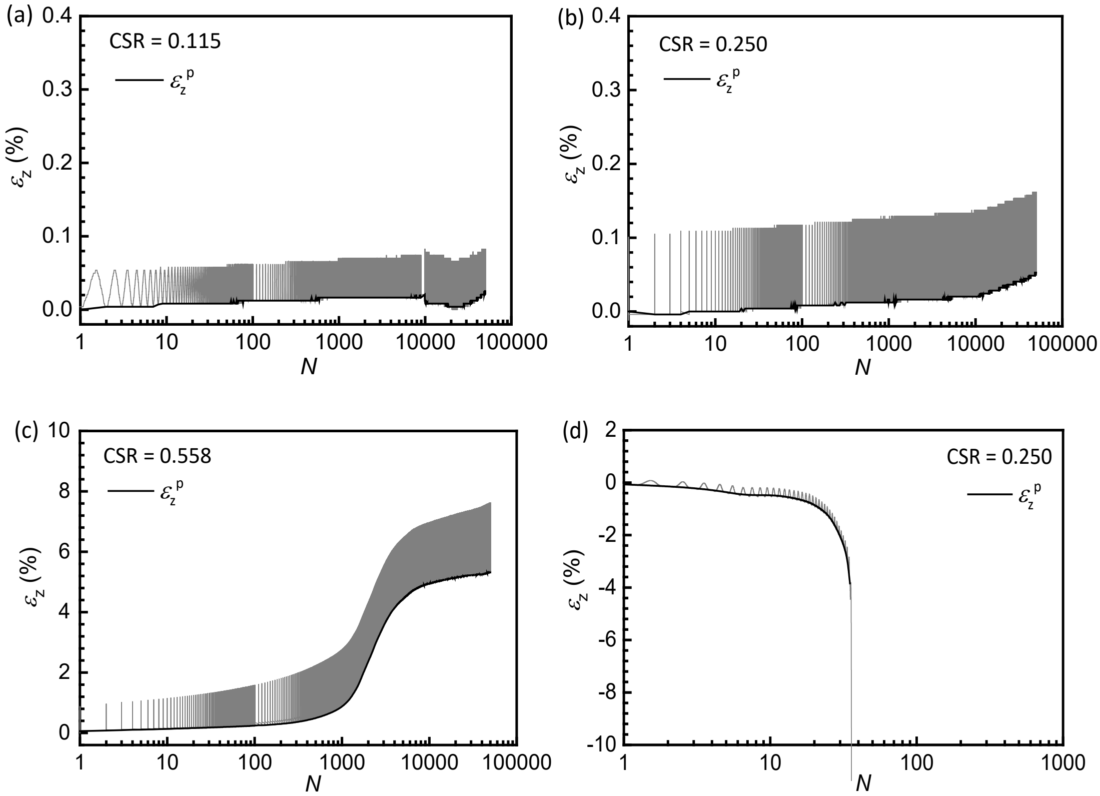


Fig. 5 Vertical strain evolutions of London clay: (a) CT test with CSR = 0.115; (b) CT test with CSR = 0.250; (c) CT test with CSR = 0.558; (d) CHCA test with CSR = 0.250

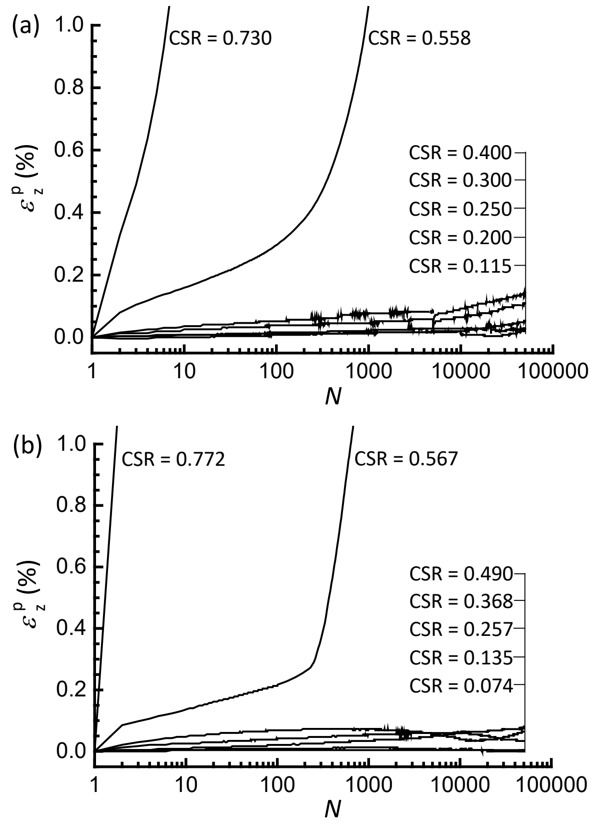


Fig. 6 Permanent vertical strain of (a) London clay in CT-I tests and (b) Kimmeridge clay in CT-II tests

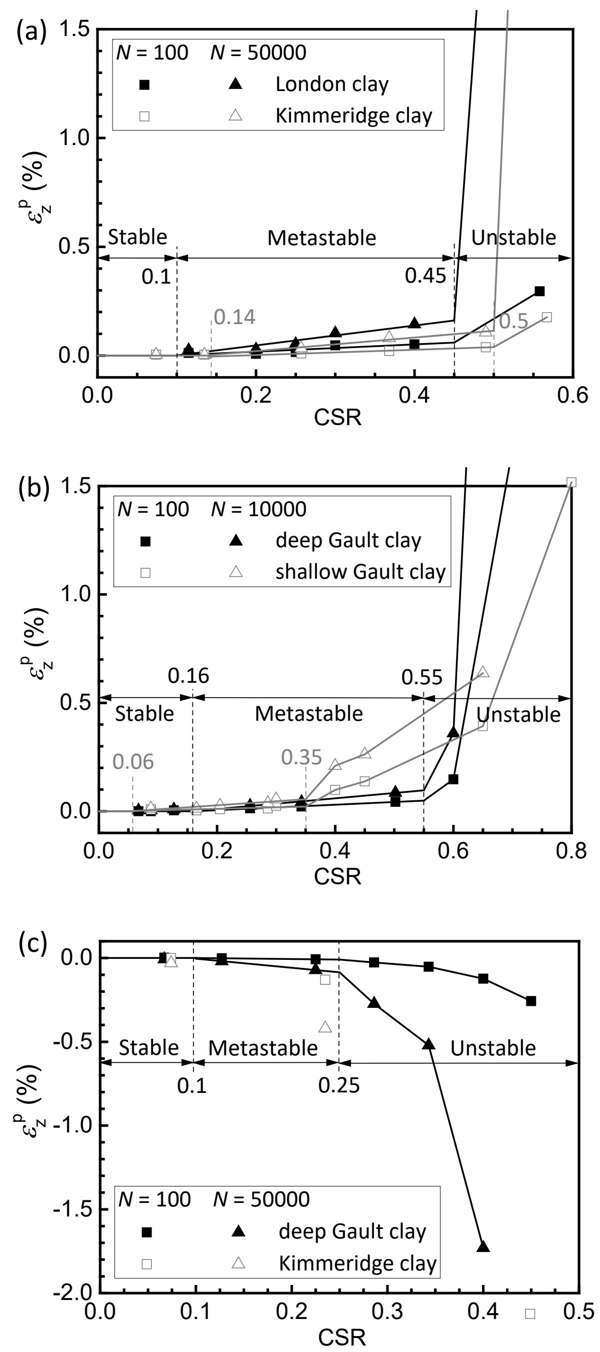


Fig. 7 Synthesis of $\varepsilon_z^p$ at specified $N$ versus CSR: (a) CT-I and CT-II tests; (b) CT-III and CT-IV tests; (c) CHCA-II and CHCA-III tests

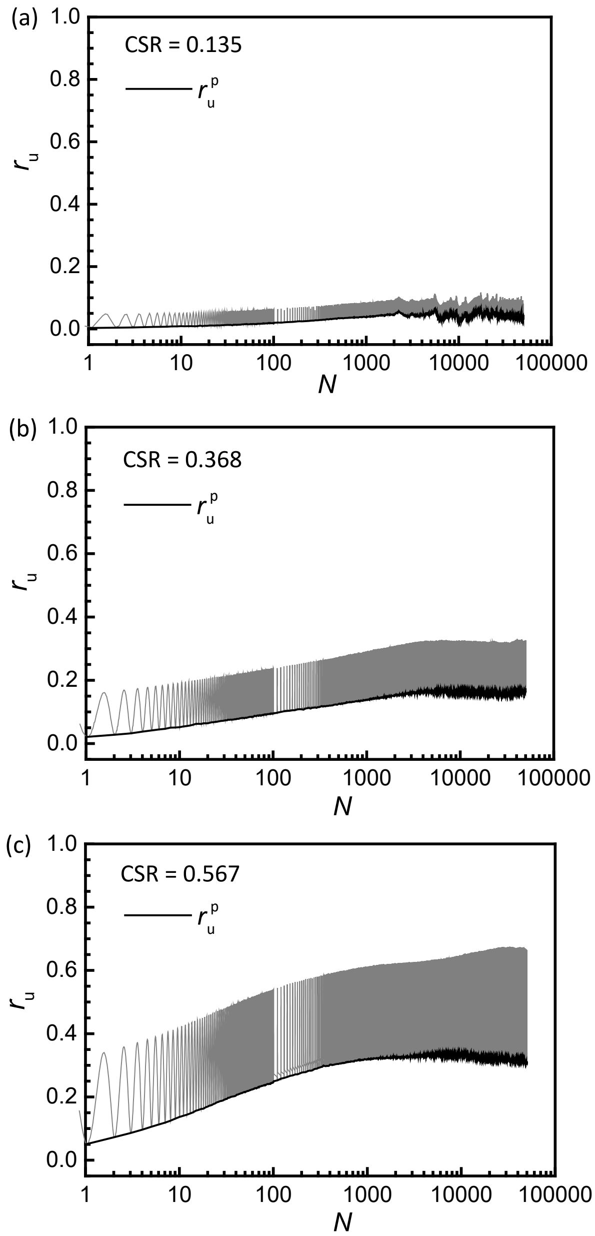


Fig. 8 Pore pressure development of Kimmeridge clay in CT-II tests: (a) CSR = 0.135; (b) CSR = 0.368; (c) CSR = 0.567

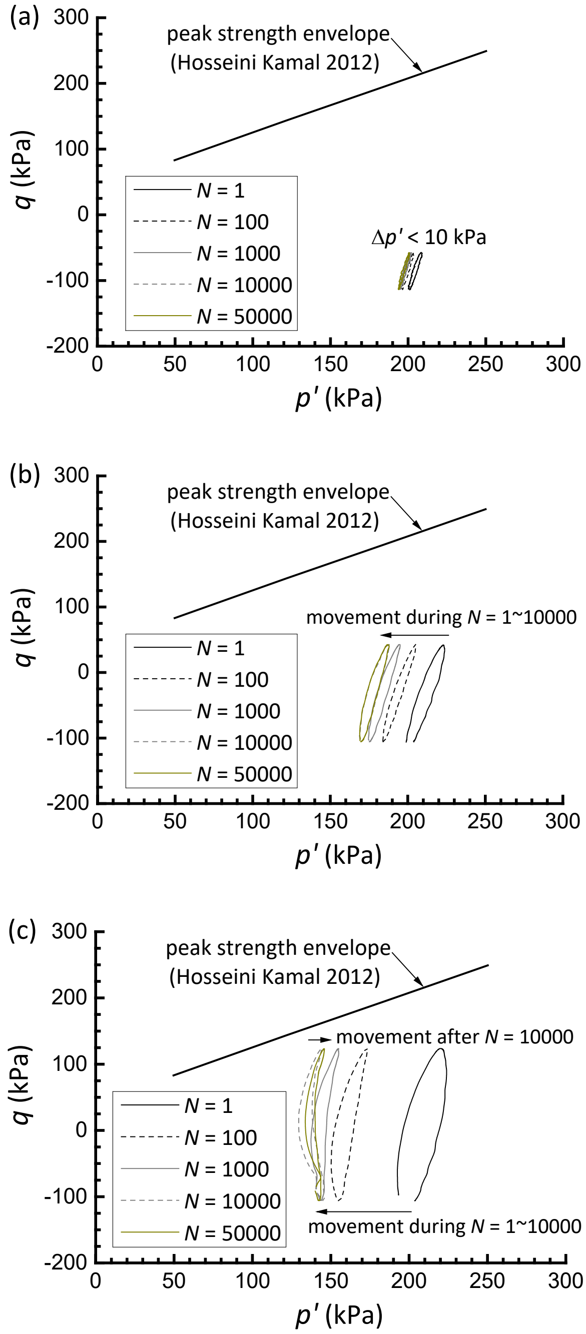


Fig. 9 Effective stress path of Kimmeridge clay in CT-II tests: (a) CSR = 0.135; (b) CSR = 0.368; (c) CSR = 0.567 (also shown is peak strength envelope identified by Hosseini Kamal (2012) from triaxial compression tests)

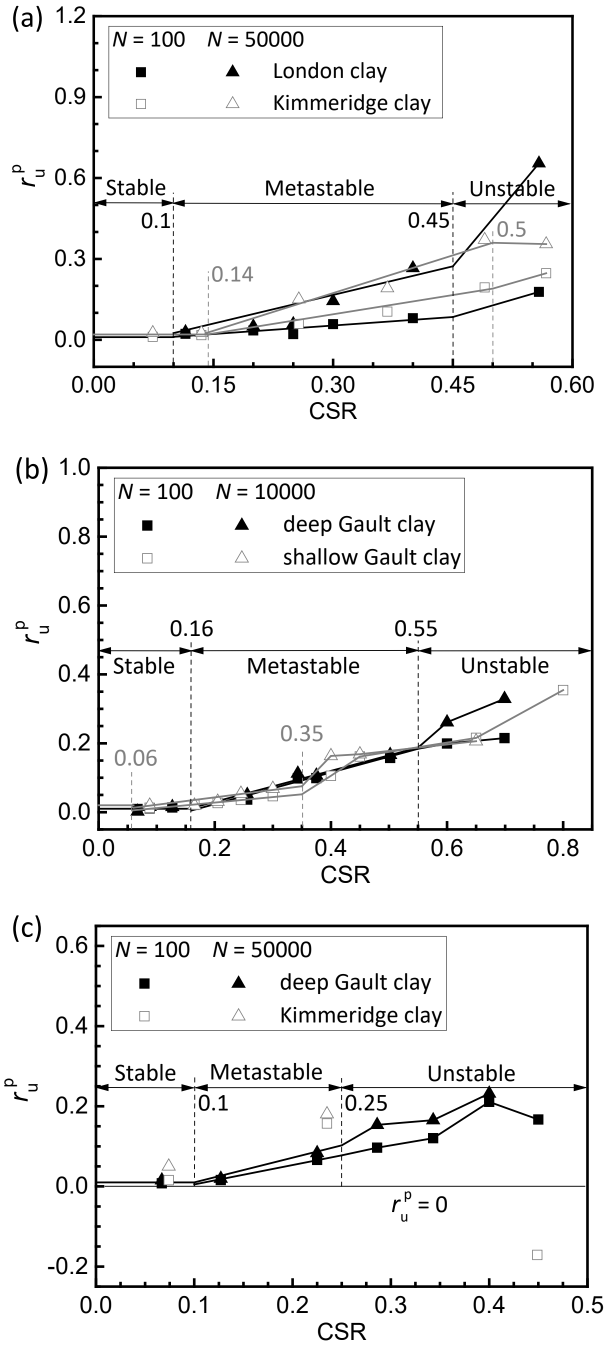


Fig. 10 Synthesis of $r_u^p$ at specified $N$ versus CSR: (a) CT-I and CT-II tests; (b) CT-III and CT-IV tests; (c) CHCA-II and CHCA-III tests

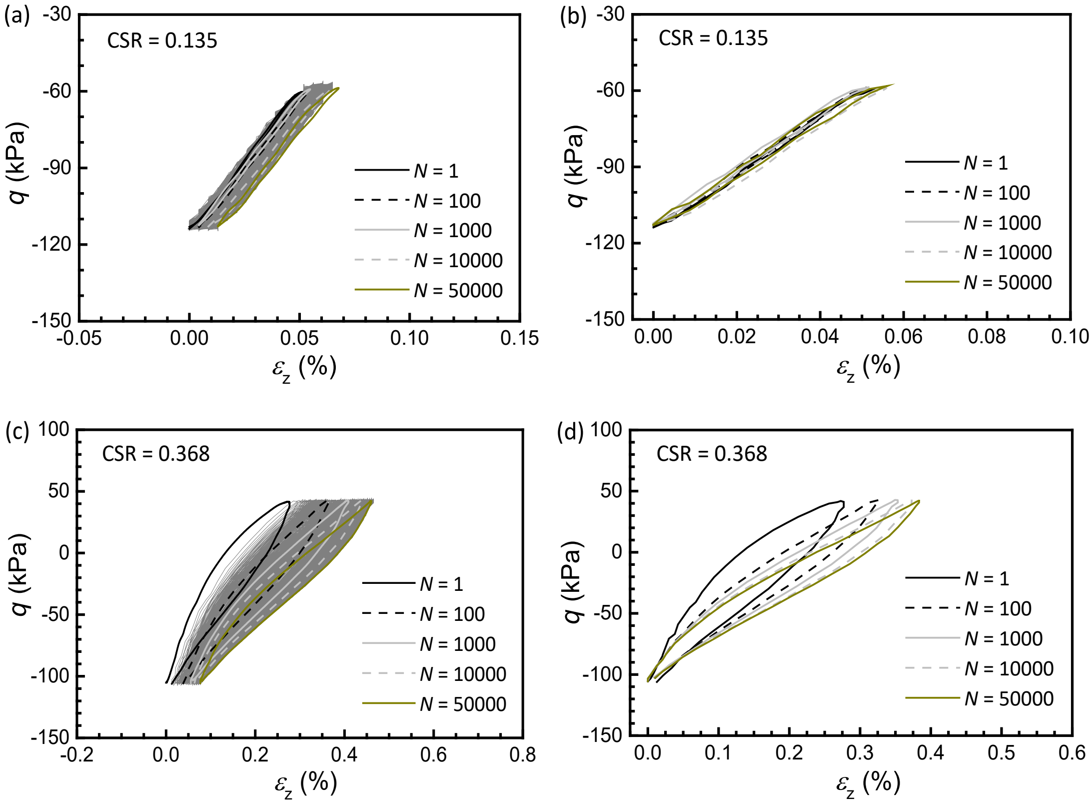


Fig. 11 Typical hysteretic response of Kimmeridge clay in CT-II tests: (a) and (c) complete vertical stress-strain loops; (b) and (d) re-zoroed vertical stress-strain loops at specified *N*

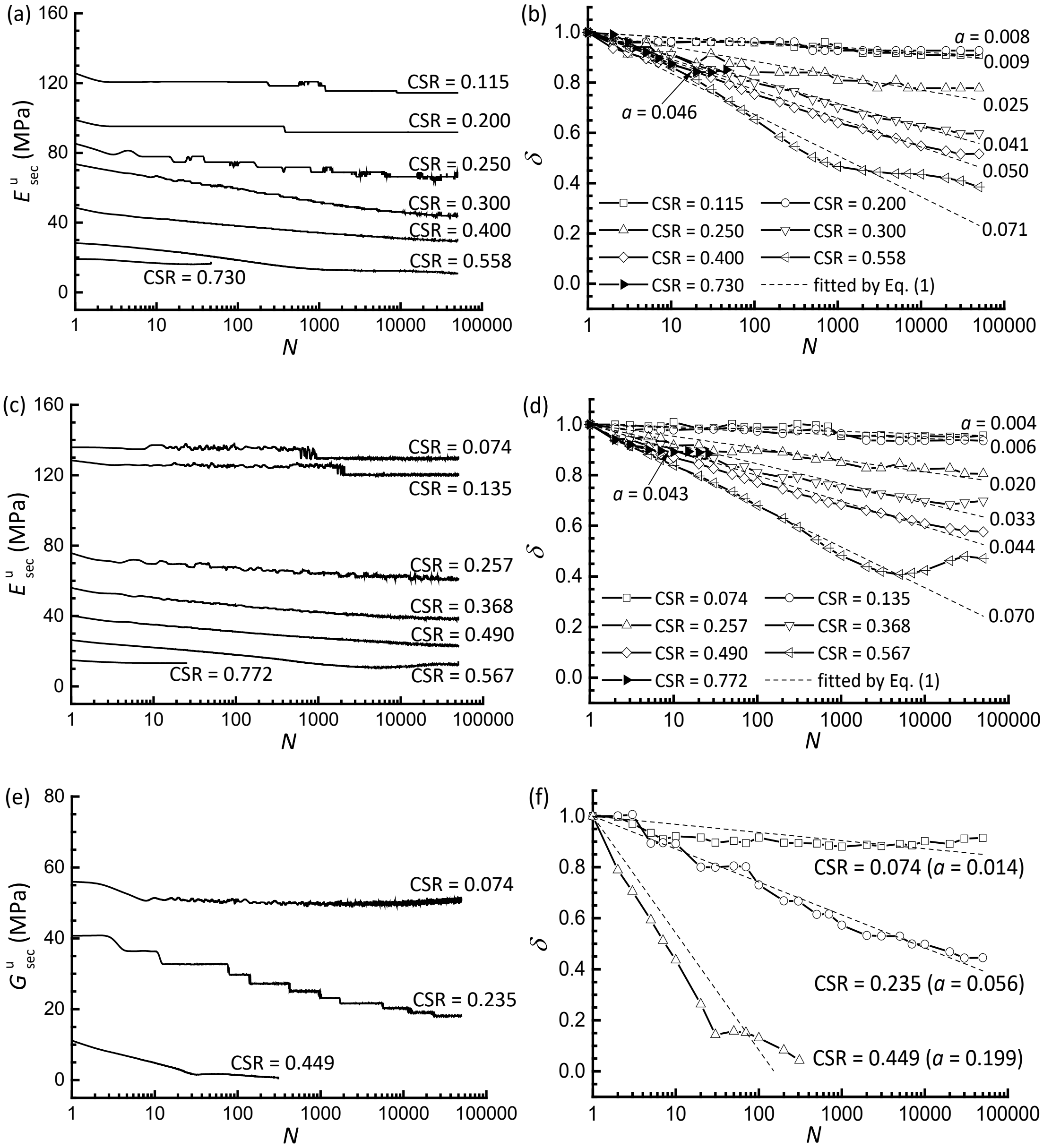


Fig. 12 Variation of cyclic secant modulus and stiffness degradation index with *N*: (a) and (b) London clay in CT-I tests; (c) and (d) Kimmeridge clay in CT-II tests; (e) and (f) Kimmeridge clay in CHCA-II tests

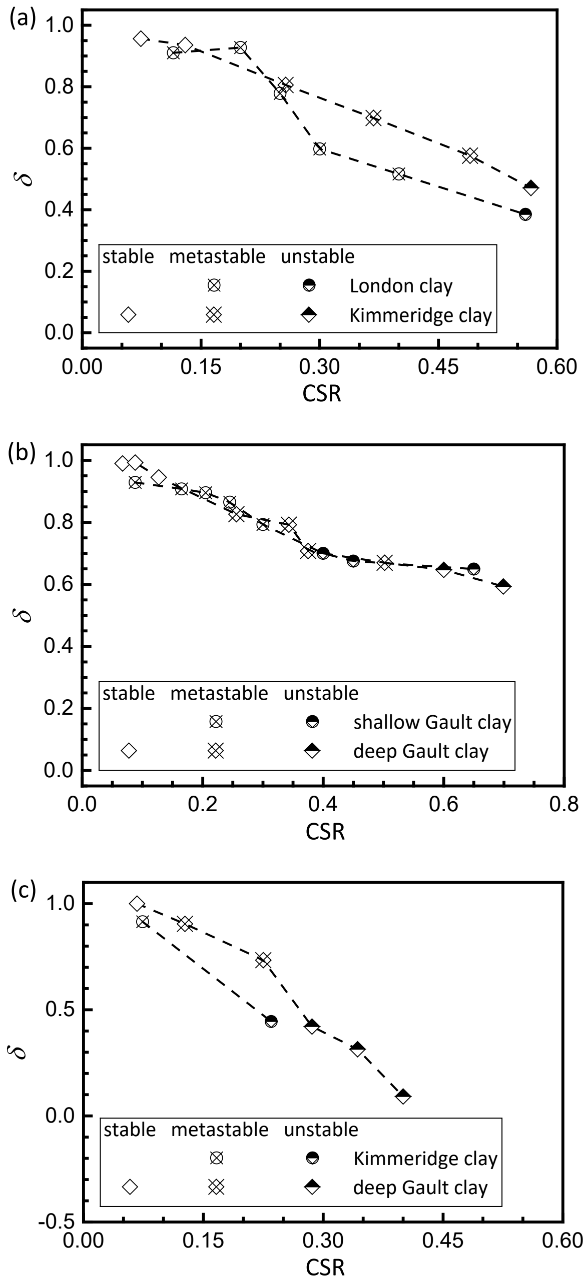


Fig. 13 Variation of stiffness degradation index at the last cycle with CSR: (a) CT-I and CT-II tests; (b) CT-III and CT-IV tests; (c) CHCA-II and CHCA-III tests

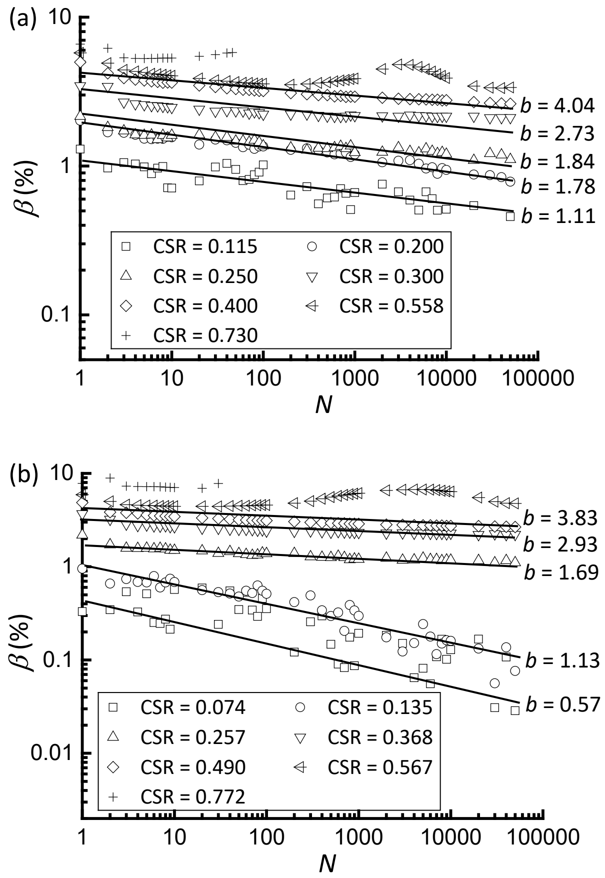


Fig. 14 Variation of damping ratio with *N*: (a) London clay in CT-I tests; (b) Kimmeridge clay in CT-II tests

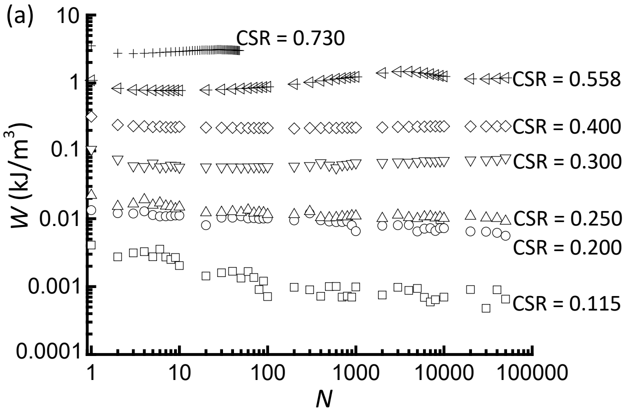


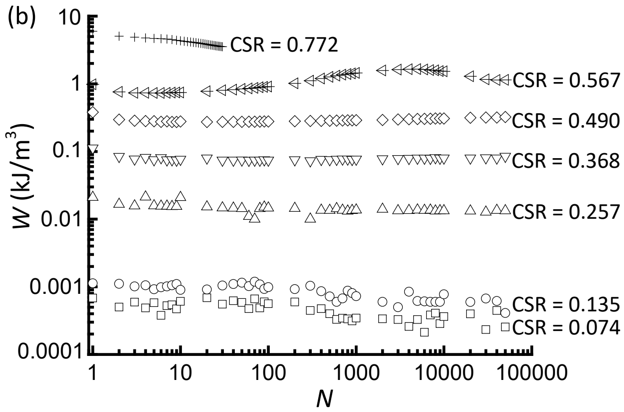


Fig. 15 Variation of dissipated energy per unit volume with *N*: (a) London clay in CT-I tests; (b) Kimmeridge clay in CT-II tests

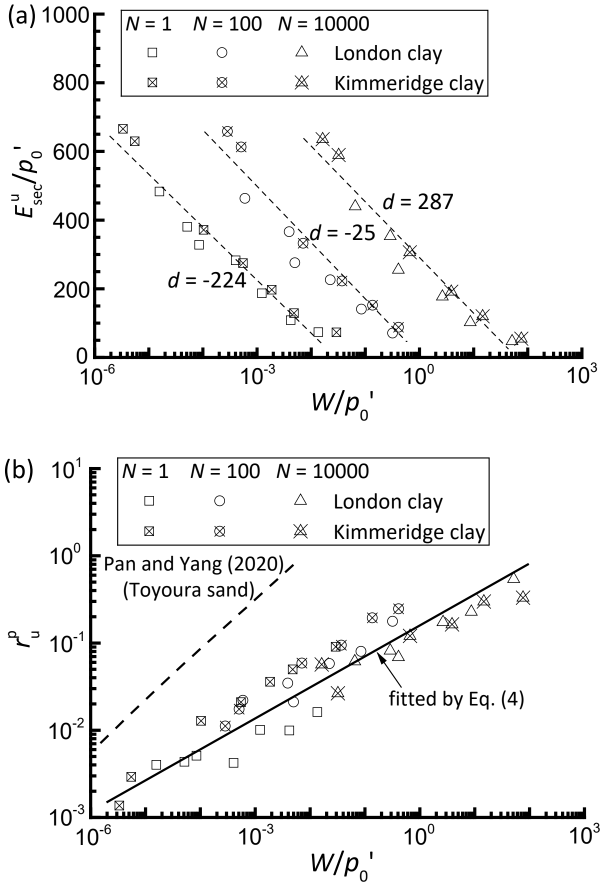


Fig. 16 (a) Normalized relationship between cyclic secant stiffness and cumulative dissipated energy; (b) permanent pore pressure ratio against normalized cumulative energy

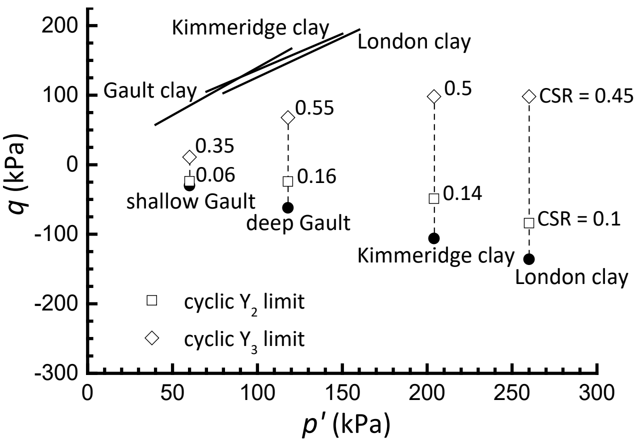


Fig. 17 Summary of cyclic yield limits interpreted from CT tests (Note: solid symbols represent in-situ $K_0$ stress states, hollow symbols represent cyclic yield points, and solid lines represent monotonic $Y_3$ yielding conditions)

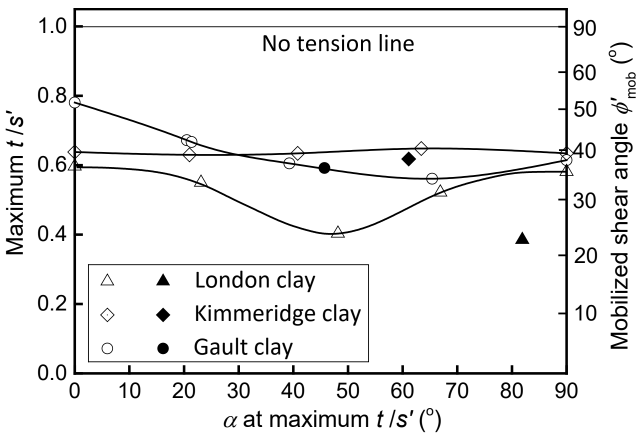


Fig. 18 Variations of maximum stress ratio $t/s'$ with $\sigma_1'$ axis orientation $\alpha$ covering both monotonic and cyclic HCA tests (Note: solid symbols represent cyclic test data and hollow symbols represent monotonic test data from Brosse et al. (2017b))